

Diffuse fraction of UV radiation under partly cloudy skies as defined by the Automated Surface Observation System (ASOS)

Richard H. Grant

Department of Agronomy, Purdue University, West Lafayette, Indiana, USA

W. Gao

U.S. Department of Agriculture UVB Monitoring and Research Program, and Cooperative Institute for Research in the Atmosphere, Colorado State University, Fort Collins, Colorado, USA

Received 14 February 2002; revised 27 September 2002; accepted 20 November 2002; published 21 January 2003.

[1] A major limitation in predicting the ultraviolet-B (UVB) irradiance on organisms is the difficulty in determining the UVB under partly cloudy sky conditions. This study developed models for estimating the diffuse fraction of ultraviolet-A (UVA) and UVB radiation under partly cloudy skies based on National Weather Service (NWS) cloud cover measurements and Department of Agriculture (USDA) UVB Radiation Monitoring and Research Network UV radiation measurements made from 1997 through 1999 at nine locations in the United States. The UVB diffuse fraction and the difference between clear and partly cloudy sky diffuse fraction were empirically modeled as a function of solar zenith angle and cloud fraction with a resulting mean bias error (MBE) of 0.019 and 0.014, respectively, and a root mean squared error (RMSE) of 0.069 and 0.079, respectively. A semiempirical model was also evaluated where the diffuse fraction was treated as the summation of clear and overcast sky diffuse fractions, respectively, weighted by the probability of the Sun's direct beam being obstructed or not for a given cloud cover fraction. This model MBE was less than 0.01 of both the UVA and UVB wave bands, while the RMSE was 0.035 within the UVB wave band and -0.030 in the UVA wave band. Model errors were greatest for low solar zenith angles and high cloud fractions in the UVB. The cloud fraction measurements used in these models only include clouds up to 3.6 km. Consequently, they should only be used when the cloud information has the same characteristics. *INDEX TERMS*: 0305 Atmospheric Composition and Structure: Aerosols and particles (0345, 4801); 0360 Atmospheric Composition and Structure: Transmission and scattering of radiation; 3359 Meteorology and Atmospheric Dynamics: Radiative processes; 3394 Meteorology and Atmospheric Dynamics: Instruments and techniques; *KEYWORDS*: UV radiation, clouds, diffuse sky radiation

Citation: Grant, R. H., and W. Gao, Diffuse fraction of UV radiation under partly cloudy skies as defined by the Automated Surface Observation System (ASOS), *J. Geophys. Res.*, 108(D2), 4046, doi:10.1029/2002JD002201, 2003.

1. Introduction

[2] A major limitation in predicting the ultraviolet-B (UVB) irradiance on humans, terrestrial plants, and aquatic organisms is the inability to specify the distribution of UVB under partly cloudy sky conditions. Many models such as that developed by Gao *et al.* [2002] and Grant *et al.* [2002] predict the irradiance under and in canopies of vegetation using separate components of diffuse sky radiance and direct beam radiance. The fraction of the global irradiance associated with the sky radiation is termed the diffuse fraction of the irradiance. UVB sky radiance distributions have been developed for cloud-free and partly cloudy skies where the Sun is visible [Grant *et al.*, 1997]. The actual intensity of the sky radiation is, however, variable under the

partly cloudy sky. So while the diffuse fraction can be readily estimated for cloud-free sky conditions or opaque (no Sun disk visible) cloudy overcast conditions, there is presently no means to readily determine the diffuse fractions for partly cloudy conditions.

[3] The relationship between diffuse fraction and cloud fraction is not linear. The diffuse fraction of the total radiation increases greatly as cloud cover increases, but increases more as the solar disk is obstructed by the clouds than when the disk is not obstructed by the clouds but the clouds are present away from the Sun. This is in part due to the differences between scattering through the cloud and off the sides of clouds [Mims and Frederick, 1994; Sabburg and Wong, 2000]. As a result, there is no direct relationship between cloud cover and diffuse fraction. An approach to estimating the above-canopy irradiance under partly cloudy skies, developed in 1999 [Grant and Heisler, 2000], uses information on the diffuse fraction under unobstructed and

Table 1. Measurement Locations and Periods of Record

Location	Location Code	Separation Distance, km	Total Observations		Cloudy Sky Observations					
			Clear	Cloudy	FEW	SCT	BKN	OVC	Elevation, m	Latitude, deg N
Baton Rouge, LA	BTR	16.0	2839	6454	1305	2055	1494	1600	7	30.4
Bledsoe Farm, GA	FFC	23.2	1702	1585	311	240	308	726	270	33.2
Grand Canyon, AZ	GCN	17.6	3040	3192	1015	594	872	711	2073	36.1
Davis, CA	SAC	26.8	4416	2398	297	372	735	994	18	38.5
Bondville, IL	CMI	11.2	3199	5977	1395	1053	1339	2190	213	40.0
Logan, UT	LGU	10.6	2352	1552	236	151	310	855	1368	41.7
Underhill, VT	MVL	23.0	4067	5669	790	606	1247	3026	408	44.5
Presque Isle, ME	CAR	18.8	2736	7003	723	836	1518	3926	144	46.7
Albion, WA	PUW	9.3	2680	4120	818	513	1152	1637	804	46.8

obstructed solar disk conditions, the frequency of obstruction of the direct beam by clouds for a given cloud fraction, and the cloud fraction.

[4] The diffuse fraction under partly cloudy skies is routinely measured by the Ultraviolet Multi-filter Rotating Shadow-band Radiometers (UV-MFRSR) and Visible Multi-filter Rotating Shadow-band Radiometers (MFRSR, Yankee Environmental Systems, Turners Falls, Massachusetts) at the United States Department of Agriculture (USDA) UV-B Radiation Monitoring and Research Program monitoring stations [Bigelow *et al.*, 1998]. Installation of the UV-MFRSR began in 1997. The instruments are now located at 28 stations across the continental United States, two locations in Canada, and one in New Zealand. The goal of the work reported here was to determine the mean UVB diffuse fraction for various sky conditions and develop a means to estimate the diffuse fraction under partial cloud cover.

2. Methods

[5] The study involved the combined analysis of the United States National Weather Service Automated Surface Observation System (ASOS) cloud cover information (hourly observations) and the USDA UVB Radiation Monitoring and Research Network (USDA UVB network) stations spectral irradiance information. Nine USDA UVB Network stations with ASOS observations made within 30 km were used in the study (Table 1). Synoptic irradiance and cloud cover measurements were assumed if the two sets of measurements were made within 10 minutes of each other.

[6] The measured diffuse fraction (D_λ) for each observation period and wave band were made using a UV-MFRSR and visible MFRSR at nine USDA UVB network stations. The visible MFRSR is a seven channel, 10-nm full width at half maximum (FWHM) filter shadow band radiometer that measures visible irradiance (total horizontal, diffuse, and direct normal) at 415-, 500-, 610-, 665-, 862-, and 940- nm nominal center wavelengths and with an additional unfiltered silicon diode [Harrison *et al.*, 1994]. The UV-MFRSR is a seven channel ultraviolet version of the MFRSR that uses 2 nm nominal FWHM bandwidth ion-assisted-deposition filters at nominal center wavelengths of 300-, 305-, 311-, 317-, 325-, 332-, and 368- nm. Each detector shares a common diffuser and different filters, thereby allowing simultaneous measurements for each passband. The instrument measures the total (no blocking) and diffuse horizontal

(direct beam blocked) irradiance within 7 seconds of one another. The direct beam component of the total irradiance is obtained by subtraction of the diffuse horizontal (S_λ) from the global horizontal irradiance (G_λ). Following the direct beam partitioning of the global irradiance measurement, the cosine response and then calibration coefficients are applied to both the direct beam and diffuse values and the global irradiance is recalculated. Global, direct, and diffuse irradiance are recorded every 20 seconds and averaged to three minute intervals.

[7] Sources of diffuse fraction measurement error include calibration drift due to sensor aging and varying response of the sensor to angular beam radiation termed the cosine or angular response. Each UV-MFRSR sensor head is calibrated and the cosine response-characterized yearly. The cosine response of each visible MFRSR has been characterized only once. The characterization of the cosine response was made by illuminating the sensor head with a direct beam varying in one-degree increments between 0 and 90° incidence along a north, south, east, and west vertical plane from the sensor center. The cosine response varied with the azimuthal orientation of the light source to diffuser, as evident in the differences between the 0 to +90° and 0 to -90° halves of the response for a given wave band. The cosine response error is the ratio of the sensor response to that of the cosine of the incidence angle of radiation (ideal response), illustrated in Figure 1. The computed direct beam was corrected for the cosine response to the Sun's direct beam using detector-specific lookup tables of the angular response [Bigelow *et al.*, 1998] with linear interpolations for the actual 3-min average solar azimuth across uncharacterized spans of 90° of azimuth. Evaluation of the 26 UV-MFRSR and the 31 visible MFRSR sensor heads for the instruments used in this study showed the diffuser response was within 10% of the ideal up to an angle of 82° and within 5% of the ideal up to an angle of 76° (Figure 1). A maximum error for the cosine response correction was estimated assuming no azimuth variation in cosine response and an atmosphere with minimal scattering. The cosine correction error was estimated as the standard deviation of the four sets of measurements of the cosine response for each sensor head. The TUV radiation model [Madronich and Flocke, 1997] was used to calculate the direct beam fraction of global irradiance in an assumed aerosol-free, 320 DU ozone column atmosphere with measurements at sea level. The error in the direct beam fraction was estimated to be less than 0.01 (1–2%) for the solar zenith angle range of 40–85° and all wave bands from 300 nm through 368 nm.

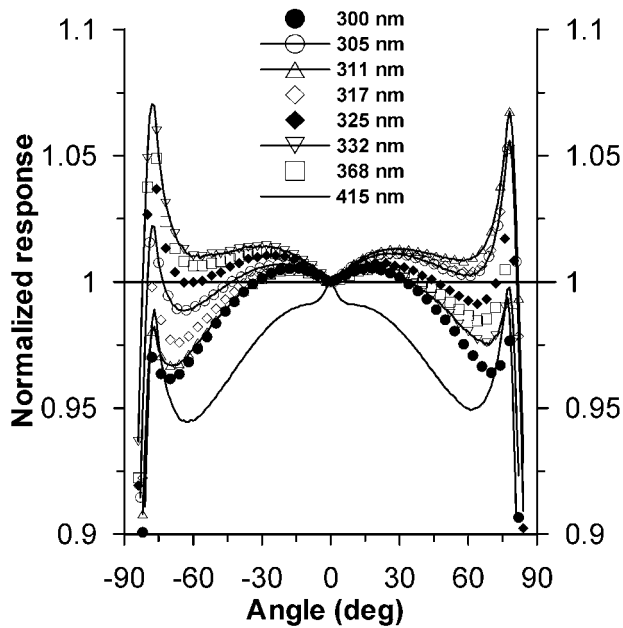


Figure 1. Mean ratio of the angular response to the ideal cosine (angular direct beam) response of the eight narrow-band channels on the UV-MFRSR and visual MFRSR instruments used in the study. The characterization of the cosine response was made illuminating the sensor head with a direct beam varying in incidence angle along azimuths of north ($-$ values), south ($+$ values), east ($-$ values), and west ($+$ values) vertical plane from the sensor center.

The measured diffuse component was cosine-response corrected assuming an isotropic sky radiance distribution resulting in an error of approximately $\pm 1.5\%$ [Grobner *et al.*, 1996]. Incorporating the direct beam and diffuse cosine correction errors resulted in an estimated diffuse fraction (D) error of approximately 0.025 (2.5%) for solar zenith angles between 40° and 85° and wave bands from 300 nm to 415 nm. The error in measured D was less than 0.025 for solar zenith angles less than 40° .

[8] Data from each day under all sky conditions were utilized during the study period. Irradiance measurements were grouped into 5° interval bins, in accordance with the approach of Frederick *et al.* [2000]. Unlike Frederick *et al.* [2000], the irradiance was not adjusted to a nominal center-of-the-bin solar zenith angle (e.g., adjusting to 22.5° for the 20° – 25° zenith angle bin) since the adjustment depends on the diffuse fraction itself. The global, direct beam, and diffuse sky spectral irradiance as well as the spectral diffuse fraction, aerosol optical depth (AOD), and total column ozone were retrieved from these spectral measurements. Diffuse fraction for the UVB wave band was defined as the mean of the 300, 305, 311, and 317 nm wave band measurements. Diffuse fraction for the ultraviolet-A (UVA) wave band was defined as the mean of the 325, 332, 368, and 415 nm wave band measurements.

[9] Mean daily values of instantaneous AOD according to Harrison and Michalsky [1994] and Rayleigh optical depth according to Bodhaine *et al.* [1999] were calculated for all days with suitable valid measurements. AOD is defined to include clouds. The total column ozone was derived accord-

ing to Gao *et al.* [2000]. Total column ozone was determined only for days with at least 5 measurements of irradiance greater than $0.0025 \text{ Wm}^{-2} \text{ nm}^{-1}$ at 311 nm. For each of those days, retrievals are made for the 5 three-minute periods with the highest irradiance measurements at 311 nm and solar zenith angles less than 70 degrees. The total column ozone reported for the day is the average of the 5 retrievals. Since the AOD can only be computed for days with significant direct beam component, these calculations were made on substantially fewer days than the total column ozone.

[10] Cloud fraction and surface air absolute humidity were determined at the time of a given set of UV measurements from an ASOS station of the National Weather Service within a distance of 30 km. The ASOS measurement of cloud cover fraction is made using a weighted average of downward scattering of a vertically oriented laser over 30 minutes, and thus represents only a partial sampling of the sky [Grant and Heisler, 2000]. Furthermore, the intensity of the ASOS laser limits the height of measurable cloud to 3.6 km; effectively excluding the detection of midlevel and high clouds. Consequently, errors in the cloud cover measurement and subsequent cloud fraction classification of radiation measurements are due to both the exclusion of clouds that do not pass over the detector in the 30-min sampling period and clouds that are above 3.6 km.

[11] The ASOS cloud cover classifications include the classes of CLear (<1 octa), FEW (1–2 octas), SCATtered (3–4 octas), BroKEN (5–7 Octas), and OverCast (8 Octas). The frequency of ASOS-defined clear sky conditions were likely overestimated at all locations since cirroform clouds are often found in otherwise clear skies and they are higher than the maximum detection height of the ASOS laser ceilometer. Based on the 1971–1981 period analysis [Warren *et al.*, 1986], cirroform clouds are present between 41 and 59% of the time over the 9 locations used in the study, while clear skies were recorded during the same period between 5% and 23% of the time (Table 2). In the present study, ASOS 'clear' conditions occurred between 28% and 65% of the valid observations, strongly suggesting cirroform cloud 'contamination' of the clear sky condition. Since cirroform clouds commonly occur with other lower cloud types, cloud fractions estimated from ASOS are also likely to be underestimated. The ASOS classification was used in this study. Note that these are not standard definitions: not only are high clouds not measured, but the ASOS clear sky definition can include some cloud cover near the horizon.

[12] The distance between radiation and cloud measurement locations introduced a source of error in the cloud fraction classification of the irradiance measurements. During periods of cloud transitions, clouds directly over the ASOS station could take 30 minutes to pass over the downwind radiation measurement location resulting in a mismatch of one hour's measurements or not pass over the radiation measurement location at all resulting in multiple hours of mismatched measurements. This error was however expected to be relatively small due to the large number of measurements used in the averaging described below (Table 1).

[13] Extensive modeling efforts have been made to predict the clear sky UVB irradiance [Stamnes *et al.*, 1988]. Instantaneous relative irradiance under partly cloudy skies

Table 2. Cloud Cover and the Probability of Unobstructed Irradiance Measurement by Location

Location Code	Study Period % Clear Skies	Climatological Mean [Warren <i>et al.</i> , 1986]		Probability of Unobstructed Beam Radiation (P_{unobs})			
		% Clear Skies	% Cirroform Clouds	FEW Clouds	SCT Clouds	BKN Clouds	OVC Clouds
BTR	31	14	57	0.78	0.64	0.43	0.09
FFC	52	18	46	0.68	0.56	0.39	0.10
GCN	49	23	51	0.83	0.64	0.35	0.14
SAC	65	16	41	0.81	0.76	0.49	0.14
CMI	35	15	49	0.70	0.56	0.35	0.05
LGU	60	13	53	0.57	0.49	0.39	0.19
MVL	42	5	48	0.47	0.41	0.27	0.12
CAR	28	5	52	0.74	0.71	0.44	0.11
PUW	39	9	59	0.73	0.63	0.36	0.10
Mean				0.70	0.60	0.39	0.12
Standard deviation				0.116	0.109	0.065	0.040

(F) was defined as the ratio of measured instantaneous cloudy irradiance ($G(\text{sky})$) to the mean measured cloud-free global irradiance for the same 5° interval of solar zenith angle,

$$F_\lambda(\text{sky}) = G_\lambda(\text{sky}) / \overline{G_\lambda(\text{clr})}, \quad (1)$$

where sky refers to a given cloud fraction and solar zenith angle range, the mean cloudy irradiance ($G_\lambda(\text{sky})$) and the mean measured cloud-free global irradiance ($G_\lambda(\text{clr})$) are for the same 5° interval of solar zenith angle. As previously stated, the global irradiance at some wavelength λ can be partitioned into the direct beam and diffuse sky components. The fraction of diffuse radiation ($D_\lambda = S_\lambda / G_\lambda$) was used to describe the diffuse radiation environment for a given cloud cover fraction at wavelength λ for each 5° interval of solar zenith angle. The diffuse fraction D for a given cloud cover fraction at wavelength λ for each 5° interval of solar zenith angle is an enhancement of the clear sky conditions.

[14] While the diffuse and direct beam components to the global irradiance are needed to determine UVB or UVA dose on organisms, knowing the fraction of diffuse radiation in combination with measured values of global UVB irradiance can also be used. Therefore it may be possible to estimate D_λ for a given cloud cover fraction using the addition of a theoretically modeled clear sky fraction and an empirically modeled difference in clear sky and partly cloudy sky diffuse fraction according to

$$\overline{D_\lambda(\text{sky})} = D_\lambda(\text{clr}) + \left(\overline{D_\lambda(\text{sky})} - \overline{D_\lambda(\text{clr})} \right), \quad (2)$$

where the two terms in the brackets on the right hand side represent the ‘diffuse fraction increment’ due to the cloud fraction. The D_{UVA} and D_{UVB} and the diffuse fraction increment of D_{UVA} and D_{UVB} were empirically modeled using solar zenith and cloud fraction as independent variables.

[15] The mean measured diffuse fraction D_λ for a given cloud cover fraction at wavelength λ for each 5° interval of solar zenith angle is a combination of the temporal average composed of periods when the Sun was visible (unobstructed by clouds) and periods of time when the Sun was not visible (cloud obstructed) according to

$$\overline{D_\lambda(\text{sky})} = \overline{D_{unobs,\lambda}(\text{sky})} P_{unobs}(\text{sky}) + \overline{D_{obs,\lambda}(\text{sky})} P_{obs}(\text{sky}), \quad (3)$$

where $D_{obs,\lambda}$ represents the diffuse fraction when the Sun is obstructed by clouds, P_{obs} is the probability of the obstruction event, $D_{unobs,\lambda}$ represents the diffuse fraction when the Sun is not obstructing the solar disk and P_{unobs} is the probability of that event occurring for a given cloud fraction. The $D_{unobs,\lambda}$ and $D_{obs,\lambda}$ terms of equation (3) include contributions from (1) scattering of direct and diffuse radiation at cloud margins, (2) multiple scattering of direct and diffuse radiation between the ground and the cloud base, and (3) scattering of direct beam and diffuse sky radiation through the cloud and in the direction of the receiving surface. The difference between $D_{unobs,\lambda}$ and $D_{obs,\lambda}$ represents the combined changes in cloud scattering associated with the change in the importance of within-cloud scattering to the diffuse fraction. Various studies have shown that scattering of cloud margins [Schafer *et al.*, 1996] and particularly scattering by cloud margins near the Sun, can play a major role in the diffuse irradiance [Sabburg and Wong, 2000; Weihs *et al.*, 2000]. The contribution of cloud penetration scattering to the mean diffuse fraction is maximized when the cloud obstructs the solar beam. We assumed that the averaging of many measurements from multiple locations resulted in a relatively uniform mean cloud depth for a given solar zenith angle and similar cloud depths and cloud droplet distributions for all cloud fractions.

[16] The probability of a sky condition having unobstructed Sun periods (P_{unobs}) or Sun obstructed periods (P_{obs}) was calculated from the entire nine-location record based on an obstructed measurement having an F_{500} value of less than 0.8 in accordance with Grant and Heisler [2000]. The mean and standard deviation of the mean (SD) diffuse fractions were determined under unobstructed, sunlit (clouds not blocking the view of the solar disk) and obstructed, shaded (clouds obscuring the solar disk) conditions for each cloud cover class and 5° interval of solar zenith angle. Errors in the P_{unobs} estimation would be expected to increase with solar zenith angle due to the increased difference between Sun position and the time-averaged vertical detection of the cloud fraction. Obstructing but undetected clouds above 3.6 km contribute to the measured variability in P_{unobs} .

[17] Estimating D_λ at unknown locations can be done either through empirical methods involving a purely empirical generalized regression function of solar zenith and latitude or through a semi-empirical method using simulated

Table 3. Description of the Meteorological Conditions During the Period of Record

Location	Clear Sky Absolute Humidity		Cloudy Sky Absolute Humidity		Aerosol Optical Depth			Ozone Column Depth		
	Mean, g m ⁻³	s.d., g m ⁻³	Mean, g m ⁻³	s.d., g m ⁻³	Mean	s.d.	n	Mean, DU	s.d., DU	n
BTR	11.81	5.64	16.32	4.34	0.700	0.116	127	293	31	677
FFC	10.66	4.90	13.10	4.36	0.679	0.118	127	277	27	696
GCN	3.44	1.49	5.75	2.65	0.466	0.053	472	312	60	800
SAC	9.69	2.79	9.23	2.86	0.667	0.090	420	317	40	686
CMI	9.92	5.00	11.11	4.86	0.649	0.079	126	300	36	599
LGU	6.08	2.36	5.68	1.90	0.560	0.066	308	299	42	721
MVL	7.87	4.24	8.83	4.04	0.622	0.081	142	332	49	666
CAR	6.94	3.79	8.13	3.79	0.624	0.067	152	322	47	586
PUW	7.07	2.27	6.76	2.13	0.600	0.073	272	317	44	622

clear sky D_λ , empirically derived probabilities of Sun obscuration during a partly cloudy period, and empirically derived corrections to account for cloud margin scattering and cloud penetration. A first and common approximation to partly cloudy skies is to assume $D_\lambda(ovc) = D_{obs,\lambda}$ and $D_\lambda(clr) = D_{unobs,\lambda}$ and that these fractions can be linearly combined to estimate the partly cloudy diffuse fraction according to

$$\overline{D_\lambda(sky)} = \overline{D_\lambda(clr)}P_{unobs}(sky) + \overline{D_\lambda(ovc)}P_{obs}(sky). \quad (4)$$

This assumes clouds with no depth (no vertical sides) that are totally opaque and do not scatter more off cloud margins than through the cloud. The accuracy of this model to describe $D_\lambda(sky)$ for a given location was evaluated using the 5° interval solar zenith angle and cloud cover fraction bin-averaged measurements for $D_\lambda(clr)$, $D_\lambda(ovc)$ and the location averaged $P_{unobs}(sky)$ and $P_{obs}(sky)$ for each cloud fraction. Variations of this model, included setting $D_\lambda(ovc)$ to 1.0 and using all-location mean values of $P_{unobs}(sky)$, were also evaluated.

[18] The empirical models were developed using measurements from locations BTR, FFC, GCN, SAC, MVL, CAR, and PUW (Table 1). The accuracy of the empirical models was estimated using measurements from two locations, CMI and LGU, representing a range in absolute humidity and AOD but similar total column ozone and latitude (Tables 1 and 3). The accuracy of the semi-empirical models based on equation (4) was estimated using all measurement locations. Models were evaluated using a measure of error variability (square root of the sum of squared mean errors; RMSE) and a measure of bias (mean bias error; MBE).

3. Results

[19] Atmospheric conditions during the radiation measurements were highly variable by location. Mean absolute humidity for the nine stations varied from 3.4 to 6.3 g m⁻³, with the humidity during the cloudy sky periods generally greater, but not with statistical significance, than that during the cloud-free days (Table 3). Mean AOD for the cloud-free days at the nine stations varied from 0.466 (GCN) to 0.700 (BTR). The coefficient of variation of AOD varied from 0.11 to 0.17. Mean total column ozone for the nine stations ranged from 277 to 332 DU (Dobson units), with variability within a given station of between 30 and 60 DU (Table 3). The coefficient of variation of total column ozone varied

from 0.10 to 0.19. The location with the greatest variability in total column ozone, the lowest AOD and the lowest absolute humidity was the Grand Canyon station (GCN). The location with the highest AOD and highest absolute humidity was the Baton Rouge station (BTR). In general, the mean AOD and mean absolute humidity for a given location were highly correlated. However, with the exception of BTR, the variability in AOD and absolute humidity were not highly correlated for a given location over the study period.

[20] For the seven locations previously indicated, F_λ ranged from a mean of 0.31 to 0.52 for overcast skies, 0.58 to 0.80 for broken skies, 0.70 to 0.93 for skies with scattered clouds, and 0.84 to 0.96 for skies with few clouds. The F_λ in the UVB wave band was less than the UVA and visible wavelengths (Figure 2), in agreement with *Grant and Heisler* [2000]. The relationship between cloud cover and F_λ was not linear. The mean change in F_λ of -0.14 octa^{-1} as cloud fraction changes from broken to overcast cover was more than twice that between the few and scattered (-0.04 octa^{-1}) or scattered to broken (-0.05 octa^{-1}) cloud cover change. The greater rate of change in F_λ between BKN and OVC skies suggests that the OVC sky had thicker clouds with less transmittance than the other cloud fractions. Since we can assume the mean conditions for all cloud fractions had some unmeasured clouds above 3.6 km, this lower transmittance of the OVC cloud fraction may be due to a greater frequency of precipitating clouds than just thicker clouds in this fraction. *Jossefson and Landelius* [2000] found that precipitating clouds had lower transmittance than nonprecipitating clouds.

3.1. Variability in Sky Diffuse Fraction

[21] The clear sky D_{UVA} for most solar zenith angles was between 0.3 and 0.7—increasing in magnitude and decreasing in variability with increased solar zenith angle (Figure 3a). All locations had similar values for a given solar zenith angle. The clear sky D_{UVB} increased with increasing solar zenith angle from 0.4 to 0.7 at zenith angles of 15° to 1.0 by a zenith angle of 75° (Figure 3b). D_λ for the clear sky conditions was probably biased high due the ASOS cloud cover measurement not detecting middle and high level clouds.

[22] In general, D_λ increased with increasing cloud fraction. However, the decline in F_λ for increasing cloud cover indicated in Figure 2 is not as evident in the diffuse fraction D_λ since the decline in G_λ with increased cloud fraction corresponds to an increase in D_λ due to the scattering of the clouds. Given the similarity in the diffuse fraction for the

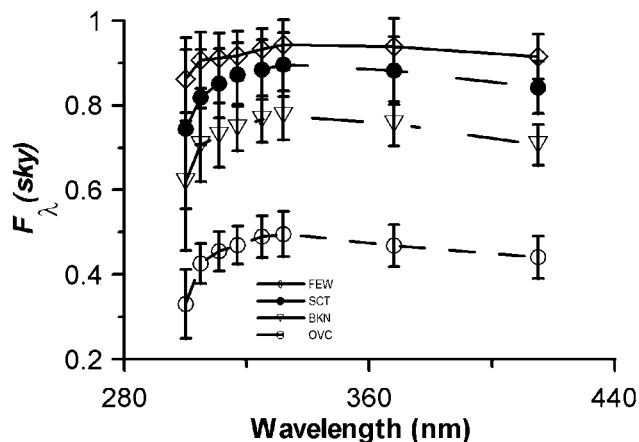


Figure 2. Mean relative irradiance under partly cloudy skies. Mean value for all solar zenith angles at locations BTR, FFC, GCN, SAC, MVL, CAR, and PUW. Bars represent the standard deviation of the mean values for each location and wavelength.

UVA and UVB wave bands, the dominant atmospheric component influencing the D_λ was probably AOD and not the total column ozone. The variability in the mean D_{UVA} and D_{UVB} for solar zenith angles between 25° and 60° was greatest when the cloud fraction was between one and 5 octas (few and scattered cloud cover classes) (Figure 4). The variability in atmospheric moisture, aerosols, and the ozone column depth decreased between locations as the air mass increased. This resulted in the decreased variability in D_λ with increased solar zenith angle. The presence of a small cover of clouds (few classification) had only a minor effect on both the D_{UVA} and D_{UVB} (Figures 2 and 4). This confirms the findings of many researchers that have shown minimal effect of clouds on the incident UVB irradiance when the fraction is less than 70% [Frederick and Steele, 1995; Nemeth et al., 1996; Thiel et al., 1997; Grant and Heisler,

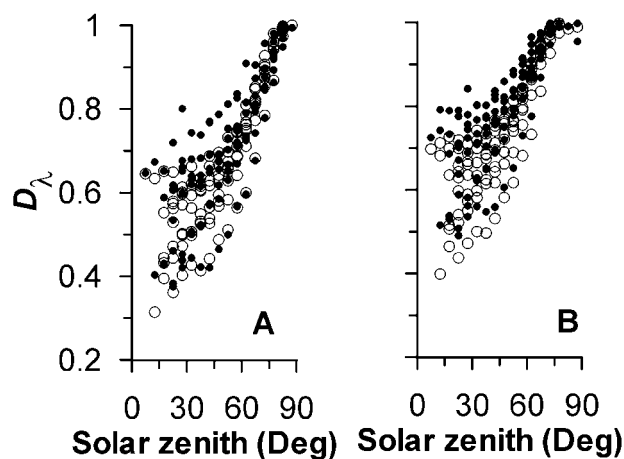


Figure 3. Diffuse fractions for UVA and UVB. The influence of solar zenith angle on the (a) UVA and (b) UVB under clear sky conditions (open circles) and skies with FEW clouds (solid circles).

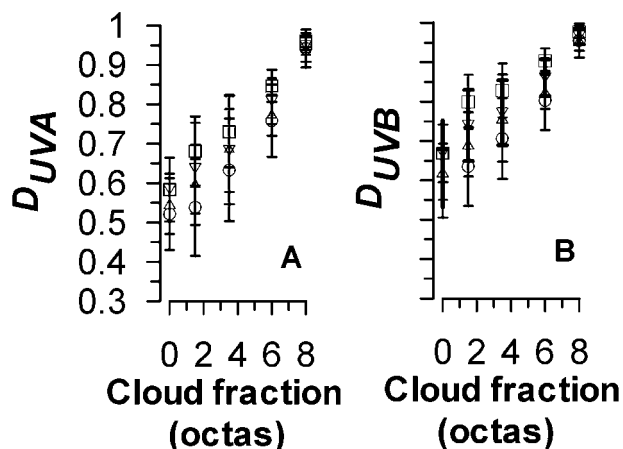


Figure 4. Mean diffuse fractions for the (a) UVA and (b) UVB wave bands relative to cloud cover. The mean values for locations BTR, FFC, GCN, SAC, MVL, CAR, and PUW with solar zenith angles between 20° – 25° (circle), 30° – 35° (triangle), 40° – 45° (inverted triangle) and 50° – 55° (square) are indicated at each cloud fraction (0 = CLR, 1.5 = FEW, 3.5 = SCT, 6 = BKN, 8 = OVC). Bars are the standard deviation of the sample.

2000]. The mean D_{UVA} and D_{UVB} for a given cloud cover fraction also varied in relationship to the mean AOD at the measurement locations. High AOD locations, such as BTR, had a greater diffuse fraction for all wavelengths than low AOD locations such as GCN. The differences in D_λ decreased with increasing cloud cover, indicating a lessening of the influence of the AOD on D_λ . As expected, the solar zenith angle influenced the rate of change in D_λ with wavelength.

3.2. Empirical Regression Models

[23] An empirical model was developed to estimate D_{UVA} and D_{UVB} based on the solar zenith angle and cloud fraction for the seven model development locations. The empirical model that was developed was a Lorentzian function of the form:

$$D_\lambda(\text{sky}) = a + b \left[\frac{1}{2} + \frac{\tan^{-1}\left(\frac{C-c}{d}\right)}{\pi} \right] - e \left[\frac{1}{2} + \frac{\tan^{-1}\left(\frac{\theta-f}{g}\right)}{\pi} \right] - h \left[\frac{1}{2} + \frac{\tan^{-1}\left(\frac{C-c}{d}\right)}{\pi} \right] \cdot \left[\frac{1}{2} + \frac{\tan^{-1}\left(\frac{\theta-f}{g}\right)}{\pi} \right], \quad (5)$$

where C is the cloud fraction and θ is the solar zenith angle. The best fit of the equation (5) model for D_{UVA} had parameters $a = 0.28$, $b = 1.059$, $c = 6.9$, $d = 2.9$, $e = 1$, $f = 69$, $g = 20$, and $h = -1.45$ and had an r^2 of 0.86. The model had a MBE of -0.033 and the RMSE of 0.065 based on the two test locations. The best fit of the equation (5) model for D_{UVB} had parameters $a = 0.053$, $b = 5.14$, $c = 14.3$, $d = 3.7$, $e = 1.3$, $f = 61$, $g = 21$, and $h = -6.99$ and had an r^2 of 0.87. The model had MBE of -0.019 and the RMSE of 0.069 for the two test locations. Much of the variability was

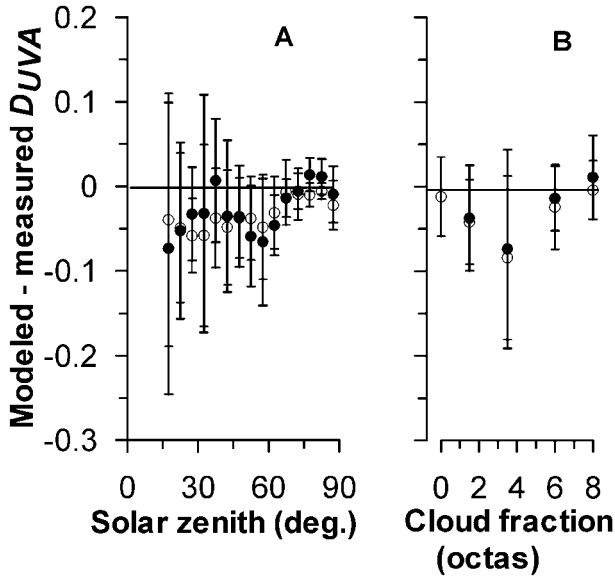


Figure 5. The model error in prediction of LGU and CMI D_{UVA} (open circles, light error bars) and $D_{UVA}(sky) - D_{UVA}(clr)$ (solid circles, dark error bars) based on values of the seven model development locations relative to the (a) solar zenith angle and (b) cloud cover fraction. Bars are the standard deviation of the model error.

presumably due to the combined effects of unmeasured middle and high level cloud cover and variability in AOD at the various locations (Table 3). The model error was greatest for midrange cloud fractions and low solar zenith angles (Figure 5).

[24] The difference between the cloudy and clear sky D_{λ} , termed the “ D_{λ} cloud increment,” was evaluated to determine if an empirical representation of equation (2) could be used to reduce variability in the estimate by extracting the typical clear sky conditions from the D_{λ} estimate. Operationally, D_{λ} could be based on modeled clear sky irradiance and cloud cover fraction. The variability in the D cloud increment (Figure 6) was less than that for D in both the UVB and UVA (Figure 4). Overall, the D_{UVA} cloud increment was greater than the D_{UVB} cloud increment under broken and overcast sky conditions; possibly due to the influence of the total column ozone on atmospheric scattering. The nonlinear relationship between cloud cover and D_{λ} cloud increment was likely a result of several factors, including scattering off clouds and multiple scattering between the clouds and the ground.

[25] The D_{UVB} and D_{UVA} cloud increments were modeled as a 6 parameter Gaussian model utilizing the calculated solar zenith angle, measured cloud fraction, and measured diffuse fractions from the seven model development locations according to

$$D_{\lambda}(sky) - D_{\lambda}(clr) = a + be^{-0.5\left(\left[\frac{c-z}{\sigma_z}\right]^2 + \left[\frac{0-z}{\sigma_\tau}\right]^2\right)}. \quad (6)$$

For the D_{UVA} cloud increment, the best fit parameters were $a = -0.031$, $b = 1.30$, $c = 17$, $d = 6.3$, $e = 28$, and $f = 30$ resulting in an r^2 of 0.85. Based on the measurements at the

two test locations, the model had a MBE of -0.028 and an RMSE of 0.079. For the D_{UVB} cloud increment, the best fit parameters were $a = -0.009$, $b = 3.73$, $c = 28$, $d = 9.4$, $e = 26$, and $f = 26$ resulting in an r^2 of 0.83. The resulting D_{UVB} cloud increment model had a MBE of -0.014 and a RMSE of 0.079. The model error for both models was greatest for midrange cloud fractions and low solar zenith angles (e.g., Figure 5). This might be expected since midrange cloud fractions are likely to have the greatest scattering off the sides of the clouds of all fractions even if the cloud aspect ratios do not change with cloud fraction. Grant and Heisler [2000] showed a secondary peak in instantaneous UVB F distributions for midrange cloud fractions that was ascribed to scattering off the ‘sides’ of clouds.

[26] The accuracy of the empirical models of UVA or UVB D_{λ} and the corresponding D_{λ} cloud increment were essentially identical and probably limited both by the complex scattering of UVA and UVB by clouds and the confounding effect of unmeasured high clouds on all cloud cover classifications. This suggests that a more mechanistic model needs to be used to improve the predictive ability of determining D_{λ} for UVB and UVA under partly cloudy skies. The components to such a model based on equations (2) through (4) are described below.

3.3. Components of the Mean Partly Cloudy Irradiance

[27] The mean global irradiance under partly cloudy skies is composed of two types of measurements: those made when the direct beam is unobstructed by clouds and those made when the clouds obstructed the direct beam radiation. The probability of having an unobstructed view of the Sun

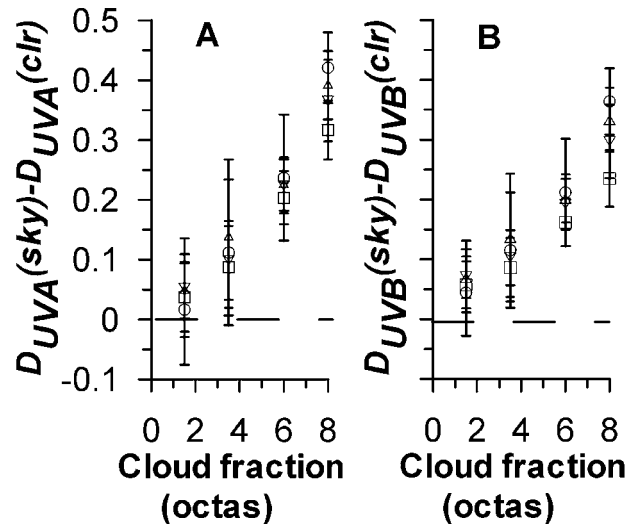


Figure 6. Mean difference in cloud-free and cloudy (FEW, SCT, BKN, OVC) sky diffuse fractions for the (a) UVA and (b) UVB wave bands relative to cloud cover. The mean values for locations BTR, FFC, GCN, SAC, MVL, CAR, and PUW with solar zenith angles between 20° – 25° (circle), 30° – 35° (triangle), 40° – 45° (inverted triangle) and 50° – 55° (square) are indicated at each cloud fraction (1.5 = FEW, 3.5 = SCT, 6 = BKN, 8 = OVC). Bars are the standard deviation of the sample.

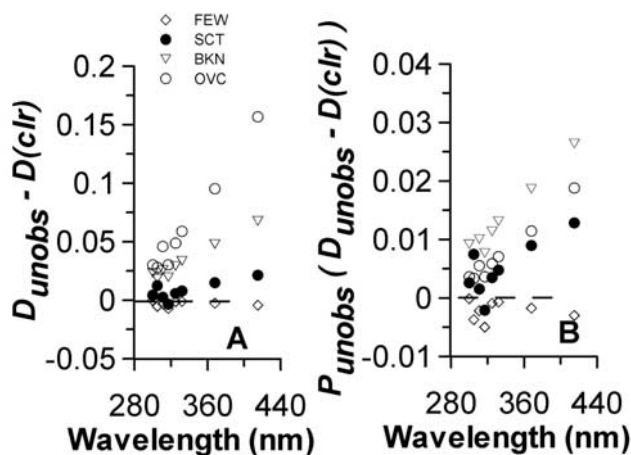


Figure 7. Difference between the unobstructed diffuse fraction and the clear sky diffuse fractions (equation (4)) for the given cloud fraction class at locations BTR, FFC, GCN, SAC, MVL, CAR, and PUW (a) without and (b) with weighting by probability of unobstructed sky.

(P_{unobs}) for a given cloud fraction varied with location of measurement. P_{unobs} was inversely related to the cloud fraction (Table 2). The mean standard deviation of the probabilities for each cloud fraction was 0.08 with increasing variability with decreasing cloud fraction (Table 2). Consequently, measurement errors in P_{unobs} were likely due to the misclassification of cloud cover by ASOS due to the spacing between the ASOS measurement and radiation measurements and the lack of detection of obstructing clouds above 3.6 km.

[28] Assuming that the averaging of many measurements from multiple locations resulted in a relatively uniform mean cloud depth for a given solar zenith angle and similar cloud depths for all cloud fractions, we can approximate $D_{unobs,\lambda}$ with the temporal mean of all measurements made during unobstructed beam radiation and $D_{obs,\lambda}$ with the temporal mean of all measurements made during periods of obstructed beam radiation. For the seven locations used for model development, the $D_{unobs,\lambda} - D_{obs,\lambda}$ value was between 0.03 and 0.04 for all cloud fractions in the UVB except OVC where the difference was 0.11. Note that $D_{unobs,\lambda}$ values for OVC cloud cover were possible since the ASOS-measured cloud cover is overhead and not necessarily in the direction of the Sun. The greater value for OVC skies is consistent with the prior discussion of the high rate of change in F_λ between BKN and OVC cloud fractions that suggested the OVC cloud fraction may have a greater frequency of precipitating clouds than the other fractions.

3.4. Two Component Probabilistic Model

[29] Estimation of $D_\lambda(clr)$ for a given location in combination with information on P_{unobs} for a given cloud fraction according to equation (3) can be used as the basis for prediction of partly cloudy diffuse fractions. Applying equation (3) requires significant on-site information concerning actual diffuse fractions under various cloud cover. To simplify the model requirements, seven of the measurement locations were used to develop approximations of the

$D_{obs,\lambda}$ and $D_{unobs,\lambda}$ assuming a mean value for $D_{obs,\lambda}$ equals the seven-location mean $D_\lambda(ovc)$ and a mean $D_{unobs,\lambda}$ equals a seven-location mean $D_\lambda(clr)$. The resulting model, equation (4), was the basis for further efforts at estimating the partly cloudy D_λ . This model further assumed that the clear sky global irradiance approximated the global irradiance of the sky with unobstructed Sun and that D_λ well-approximated $D_{unobs,\lambda}$.

[30] The above assumptions ignore the radiation under partly cloudy skies that comes from scattering off of cloud margins near the Sun [Schafer et al., 1996; Sabburg and Wong, 2000] and from the multiple scattering between the ground and the cloud cover. Are these contributions to the modeled partly cloudy D_λ significant? Combining all locations, the tendency of increased D_λ of the unobstructed sky with increasing cloud fraction was evident. D_{unobs} was approximately the same as $D_\lambda(clr)$ for the FEW and SCT cloud fractions (-0.005 to $+0.002$) but exceeded $D_\lambda(clr)$ for the BKN and OVC cloud fractions (Figure 7). This additional scattering under unobstructed periods of the partly cloudy day for high cloud fractions may explain the model overestimate for the BKN and OVC sky conditions illustrated in Figure 7. For a given location, the FEW, SCT and BKN cloud fraction classes all had a mean value of D_λ for λ between 300 nm and 325 nm within 0.04 of clear sky conditions when the Sun was unobstructed, with none of the differences significantly different ($p = 0.05$) from each other. Differences between $D_\lambda(clr)$ and $D_{unobs,\lambda}$ were greater for low AOD locations such as GCN than high AOD locations such as BTR. There was a linear trend of increasing difference between $D_{unobs,\lambda}$ and $D_\lambda(clr)$ with increasing wavelength (Figure 7a). The differences between $D_\lambda(clr)$ and $D_{unobs,\lambda}$ were less in the UVB wavelengths than the UVA wavelengths for all cloud fractions (Figure 7a). These differences are likely due to the effects of unmeasured high clouds and scattering off the measured clouds. A corresponding estimate of this scattering by Grant and Heisler [2000] was nearly twice as large. This might be expected

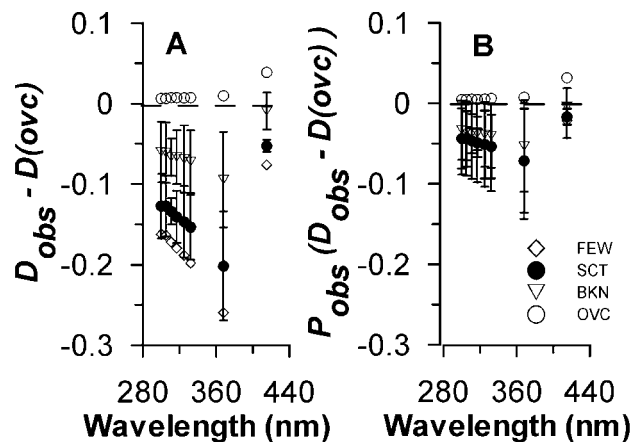


Figure 8. Difference between the obstructed diffuse fraction and the overcast sky diffuse fractions (equation (4)) for the given cloud fraction class for locations BTR, FFC, GCN, SAC, MVL, CAR, and PUW (a) without and (b) with weighting by probability of unobstructed sky.

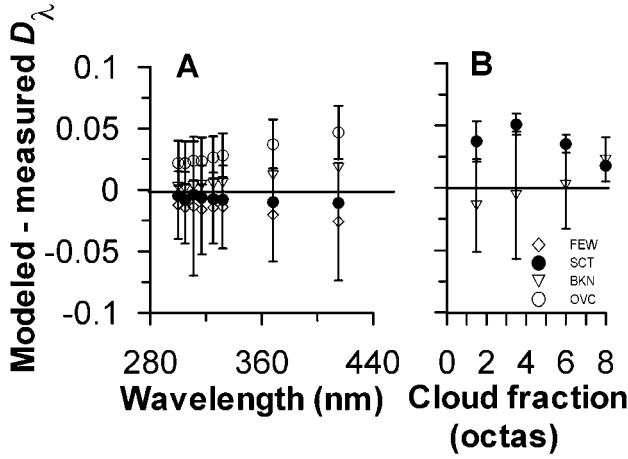


Figure 9. Model error for the two component model with respect to (a) wavelength and (b) cloud fraction. Bars are standard deviations of the error.

since $D_{unobs,\lambda} - D_{\lambda}(clr)$ was likely underestimated due to the height limitation of the ASOS cloud cover measurement.

[31] The overcast sky global irradiance and $D_{\lambda}(ovc)$ were expected to approximate the global irradiance of the sky and $D_{obs,\lambda}$ when the solar beam was obstructed. The assumption of $D_{obs,\lambda} = D_{\lambda}(ovc)$ was tested for the seven locations. $D_{obs,\lambda}$ for each cloud cover class approximated $D_{\lambda}(ovc)$ (Figure 8a), with the greater cloud cover better approximating the overcast condition. Although $D_{obs,\lambda}$ was less for partial cloud cover than OVC, the temporal mean $G_{obs,\lambda}$ was higher. The difference between $D_{obs,\lambda}$ and $D_{\lambda}(ovc)$ was not correlated with the mean AOD or absolute humidity. While significant differences ($p = 0.05$) between the $D_{obs,\lambda}$ and $D_{\lambda}(ovc)$ were evident in the UV wavelengths at some locations, $D_{obs,\lambda}$ in each cloud class did not significantly vary across the wave band of 300 to 332 nm for the combined data set. This may have been partly due to some locations having more unmeasured cloud cover above 3.6 km than other locations. The mean difference between $D_{obs,\lambda}$ and $D_{\lambda}(ovc)$ in the UVB wave band was -0.17 for FEW cloud cover, -0.13 for SCT cloud cover, -0.06 for BKN, and 0.00 for OVC cloud cover. Deviations of the $D_{obs,\lambda}$ from $D_{\lambda}(ovc)$ decreased with increasing cloud fraction (Figure 8a). The tendency for the $D_{obs,\lambda}$ at lower cloud covers to have greater differences from the OVC indicated substantial scattering through the cloud cover obstructing the direct beam and scattering by the clouds away from the Sun.

[32] The model defined by equation (4) was evaluated using the location-specific probabilities of cloud obstruction of the direct beam radiation. This model tended to overestimate the D_{λ} of the skies with OVC and BKN cloud fractions and slightly underestimate the D_{λ} for the skies with the FEW and SCT cloud classes (Figure 9). Within the UVB wave band, the model MBE was 0.001 while the RMSE was 0.035 . Within the UVA wave band, the model MBE was 0.003 and the RMSE was -0.030 . For all wavelengths and cloud classes combined, the MBE and RMSE of the model was 0.004 and 0.037 , respectively. The RMSE of both wave bands and all wavelengths were largely accounted for by the expected 0.025 error in the measured D_{λ} . The RMSE was linearly correlated with the variability in AOD ($r = 0.61$) with the greatest errors at low solar zenith angles where spacing between the radiation and cloud fraction measurements would have their greatest impact. The assumption of $D_{unobs,\lambda} = D_{\lambda}(clr)$ resulted in errors in the modeling of the term $P_{unobs}D_{unobs,\lambda}$ in equation (3) that lay between -0.005 to $+0.03$ (Figure 7b). The assumption that $D_{obs,\lambda} = D_{\lambda}(ovc)$ resulted in errors in the modeling of the term $P_{obs}D_{obs,\lambda}$ in equation (3) of between -0.07 to $+0.03$ (Figure 8b). The tendency for the $D_{obs,\lambda}$ at lower cloud cover to have greater differences from the OVC than at higher cloud cover may explain the underestimation of the equation (3) model (Figure 7) but clearly will not account for the overestimation of D_{λ} under OVC skies.

[33] The two component model of equation (5) was simplified by assuming $D_{obs,\lambda} = 1.0$ instead of using location and cloud fraction-specific values for $D_{\lambda}(ovc)$ since theoretically we would expect $D_{\lambda}(ovc) = 1.0$ and since $D_{obs,\lambda}$ was within $+0.01$ to -0.05 of $D_{\lambda}(ovc)$ in the UVB wave band. This simplified model,

$$D_{\lambda}(sky) = D_{\lambda}(clr)P_{unobs}(sky) + [1 - P_{unobs}(sky)], \quad (7)$$

was nearly as accurate as the location-specific model described above. For all locations and cloud classes combined, the MBE for both the UVA and UVB wave band was -0.003 while the RMSE was 0.04 for the UVB wave band and 0.03 for the UVA wave band. Further simplifying the equation (7) model by using the mean values of $P_{unobs}(sky)$ from Table 2 resulted in a decrease in accuracy to a RMSE of 0.05 and MBE of 0.01 for the UVB wave band and a RMSE of 0.06 and MBE of 0.03 for the UVA wave band. This accuracy is approximately that of the empirical model of equation (5). This indicates that without also having location-specific values for $P_{unobs}(sky)$, the use of location-specific values for $D_{\lambda}(clr)$ does not contribute to

Table 4. Model Summary

Model Output	Model	Model Inputs	Parameters
D_{UVB}, D_{UVA}	equation (4)	Locally measured $P_{unobs}(C)$ Locally measured $D_{\lambda}(clr)$ Locally measured $D_{\lambda}(ovc)$	None
D_{UVB}, D_{UVA}	equation (5)	ASOS derived C θ	In text
D_{UVB}, D_{UVA}	equation (7)	$P_{unobs}(C)$ from Table 2 or local measurements Locally measured $D_{\lambda}(clr)$	None
D_{UVB}, D_{UVA} cloud increment	equation (6)	ASOS derived C θ	In text

the accurate modeling of partly cloudy D_{UVA} or D_{UVB} . Differences in the frequency of occurrence of a given cloud type and the presence of unmeasured mid and upper level clouds between locations probably limit the accuracy of such generalized models.

4. Conclusions

[34] Three models were developed in this study (Table 4). The differences in the accuracy of estimating D_{UVA} and D_{UVB} with a given model were small. Of the two models developed to estimate the diffuse fraction of UVA and UVB under partly cloudy skies, the two component semiempirical model of equation (7) was more accurate than the empirical model of equation (5). Although less accurate than the two-component model, the empirical model of the solar UV diffuse fraction under partly cloudy skies required fewer measured values than the two-component model (Table 4). In the absence of location-specific values for $P_{unobs}(sky)$, the empirical model provided as accurate an estimate of partly cloudy D_{UVA} or D_{UVB} as the two-component model. It is recommended that the empirical models of D_{UVA} or D_{UVB} be used unless location-specific information on $P_{unobs}(sky)$ for all cloud fractions and clear sky D_{UVA} or D_{UVB} is available. If the location-specific information is available, then the two-component model of equation (7) should be used. Care needs to be used when using the models developed here for a specific location since the models are based on the use of USA National Weather Service ASOS observations that do not measure clouds higher than 3.6 km.

[35] **Acknowledgments.** Thanks go to Dave Bigelow, who died June 10, 2000, for his quality assurance of the data used in this study. Research was funded in part by the Purdue Agricultural Experiment Station and USDA agreement 99-34263-8566. This paper is journal paper 16631 of the Purdue Agricultural Experiment Station.

References

- Bigelow, D. S., J. R. Slusser, A. F. Beaubien, and J. H. Gibson, The USDA Ultraviolet Radiation Monitoring Program, *Bull. Am. Meteorol. Soc.*, 79, 601–615, 1998.
- Bodeker, G. E., and R. L. McKenzie, An algorithm for inferring surface UV irradiance including cloud effects, *J. Appl. Meteorol.*, 35, 1860–1877, 1996.
- Bodhaine, B. A., E. G. Dutton, N. B. Wood, and J. R. Slusser, Note on Rayleigh optical depth calculations, *J. Atmos. Oceanic Technol.*, 16, 1854–1861, 1999.
- Frederick, J. E., and H. D. Steele, The transmission of sunlight through cloudy skies: An analysis based on standard meteorological information, *J. Appl. Meteorol.*, 34, 2755–2761, 1995.
- Frederick, J. E., J. R. Slusser, and D. S. Bigelow, Annual and interannual behavior of solar ultraviolet irradiance revealed by broadband measurements, *Photochem. Photobiol.*, 72, 488–496, 2000.
- Gao, W., J. R. Slusser, J. H. Gibson, G. Scott, D. S. Bigelow, J. Kerr, and B. McArthur, Direct-sun ozone retrieval by the UV multi-filter rotating shadowband radiometer and comparison with those from Brewer and Dobson spectrophotometers, *Appl. Opt.*, 40, 3149–3155, 2000.
- Gao, W., R. H. Grant, and G. M. Heisler, A geometric UV-B radiation transfer model applied to agricultural vegetation canopies, *Agron. J.*, 94, 475–482, 2002.
- Grant, R. H., and G. M. Heisler, Obscured overcast sky radiance distributions for the ultraviolet and photosynthetically-active radiation wavebands, *J. Appl. Meteorol.*, 36, 1336–1345, 1997.
- Grant, R. H., and G. M. Heisler, Estimation of ultraviolet-B irradiance under variable cloud conditions, *J. Appl. Meteorol.*, 39, 904–916, 2000.
- Grant, R. H., G. M. Heisler, and W. Gao, Ultraviolet sky radiance distributions of translucent overcast skies, *J. Theor. Appl. Climatol.*, 58, 129–139, 1997.
- Grant, R. H., G. M. Heisler, and W. Gao, Estimation of pedestrian level UV-B exposure under trees, *Photochem. Photobiol.*, 75, 369–376, 2002.
- Grobner, J., M. Blumthaler, and W. Ambach, Experimental investigation of spectral global irradiance measurement errors due to a nonideal cosine response, *Geophys. Res. Lett.*, 23, 2493–2496, 1996.
- Harrison, L., and J. Michalsky, Objective algorithms for the retrieval of optical depths from ground-based measurements, *Appl. Opt.*, 33, 5126–5132, 1994.
- Harrison, L., J. Michalsky, and J. Berndt, Automated multi-filter rotating shadowband radiometer: An instrument for optical depth and radiation measurements, *Appl. Opt.*, 33, 5118–5125, 1994.
- Jossefson, W., and T. Landelius, Effect of clouds on UV irradiance: As estimated from cloud amount, cloud type, precipitation, global radiation, and sunshine duration, *J. Geophys. Res.*, 105, 4927–4935, 2000.
- Madronich, S., and S. Flocke, Theoretical estimation of biologically effective UV radiation at the Earth's surface, in *Solar Ultraviolet Radiation—Modeling, Measurements and Effects*, NATO ASI Ser. I, Global Environ. Change, vol. 52, edited by C. S. Zerefos and A. F. Bais, pp. 23–48, Springer-Verlag, New York, 1997.
- Mims, F. M., and J. E. Frederick, Cumulus clouds and UV-B, *Nature*, 371, 291, 1994.
- Nemeth, P., Z. Toth, and Z. Nagy, Effect of weather conditions on UV-B radiation reaching the earth's surface, *J. Photochem. Photobiol. B, Biology*, 32, 177–181, 1996.
- Sabburg, J., and J. Wong, The effect of clouds on enhanced UVB irradiance at the earth's surface: A one year study, *Geophys. Res. Lett.*, 27, 3337–3340, 2000.
- Schafer, J. S., V. K. Saxena, B. N. Wenny, W. Barnard, and J. J. DeLuisi, Observed influence of clouds on ultraviolet-B radiation, *Geophys. Res. Lett.*, 23, 2625–2628, 1996.
- Stamnes, K., S.-C. Tsay, W. Wiscombe, and K. Jayaweera, Numerically stable algorithm for discrete ordinate method radiative transfer in multiple scattering and emitting layered media, *Appl. Opt.*, 27, 2502–2509, 1998.
- Thiel, S., K. Steiner, and H. K. Seiditz, Modification of global erythemally effective irradiance by clouds, *Photochem. Photobiol.*, 65, 969–973, 1997.
- Warren, S. G., C. J. Hahn, J. London, R. M. Chervin, and R. L. Jenne, Global distribution of total cloud cover and cloud type amounts over land, *NCAR Tech. Note TN-273+STR.*, Natl. Cent. for Atmos. Res., Boulder, Colo., 1986. (Available from Natl. Tech. Inf. Serv., Springfield, Va.)
- Weih, P., A. R. Webb, and G. W. Middleton, Measurements of the diffuse UV sky radiance during broken cloud conditions, *J. Geophys. Res.*, 105, 4937–4944, 2000.
- Ziemke, J. E., J. R. Herman, J. L. Stanford, and P. K. Bartia, Total ozone/UVB monitoring and forecasting: impact of clouds and the horizontal resolution of satellite retrievals, *J. Geophys. Res.*, 103, 3865–3871, 1998.
- W. Gao, USDA UVB Monitoring and Research Program, and Cooperative Institute for Research in the Atmosphere, Colorado State University, Fort Collins, CO 80523, USA.
- R. H. Grant, Department of Agronomy, Purdue University, 1150 Lilly Hall, West Lafayette, IN 47907-1150, USA. (rgrant@purdue.edu)